Modeling the evolution of crystallographic dislocation density in crystal plasticity

Athanasios Arsenlis[1], David M. Parks[*]

*Department of Mechanical Engineering, Massachusetts Institute of Technology,
77 Massachusetts Avenue, Room 1-308, Cambridge, MA 01239, USA*

Abstract

Dislocations are the most important material defects in crystal plasticity, and although dislocation mechanics has long been understood as the underlying physical basis for continuum crystal plasticity formulations, explicit consideration of crystallographic dislocation mechanics has been largely absent in working constitutive models. Here, dislocation density state variables evolve from initial conditions according to equations based on fundamental concepts in dislocation mechanics such as the conservation of Burgers vector in multiplication and annihilation processes. The model is implemented to investigate the polyslip behavior of single-crystal aluminum. The results not only capture the mechanical stress/strain response, but also detail the development of underlying dislocation structure responsible for the plastic behavior. © 2002 Elsevier Science Ltd. All rights reserved.

1. Introduction

Dislocations, through their conservative motion on slip planes, provide a mechanism for plastic deformation in crystals, and interactions between dislocations account for much of the strength of crystalline materials. Yet dislocation mechanics has played a relatively small role in continuum crystal plasticity models. Although the physical basis

---

[*] Corresponding author. Fax: +1-617-258-8742.

E-mail address: dmparks@mit.edu (D.M. Parks).

[1] Currently, Lawrence Livermore National Laboratory, Livermore, CA, USA.

for all crystal plasticity formulations is rooted in dislocation mechanics, dislocations, in the form of densities, rarely appear explicitly in working models.

Internal state variables provide a powerful continuum constitutive modeling framework. In continuum crystal plasticity, the material state is most often described by a set of parameters representing slip-system-based deformation resistance (strength), rather than by dislocation density (structure). The strengths evolve with plastic slip according to a prescribed hardening rule. Much of crystal plasticity research has focused on developing phenomenological hardening rules to describe the plastic behavior of crystals (Franciosi and Zaoui, 1982; Follansbee and Kocks, 1988; Bassani and Wu, 1991; Qin and Bassani, 1992; Kothari and Anand, 1998; Marin and Dawson, 1998; Nemat-Nasser et al. 1998a,b; Balasubramanian and Anand, 2000). Given the complex relations between dislocation structure and deformation resistance, it is not surprising that the successes of traditional approaches to the development of phenomenological relations describing the evolution of deformation resistances have been circumscribed.

Strength-based crystal plasticity models have successfully predicted stress/strain response and texture evolution of polycrystals for a wide range of strain rates and temperatures (Mathur and Dawson, 1989; Bronkhorst et al., 1992; Beaudoin et al., 1994; Nemat-Nasser et al., 1998a,b; Kumar and Dawson, 1998). However, in detailed inspections of simulation results, the predictions of strength-based crystal plasticity models have failed to capture the local plastic response (Becker and Panchanadeeswaran, 1995), and they have been mostly unsuccessful in capturing the orientation dependence of the stress/strain behavior of single crystals (Kumar and Yang, 1999). Also, crystallographic strengths cannot be directly observed, and validation of hardening proposals requires experimental data that is difficult to obtain (Kocks and Brown, 1966; Bassani and Wu, 1991).

Underlying the phenomenology of strength-based models are dislocation processes governing the evolution of the strength variables. The crystallographic strengths quantify the resistance that gliding dislocations encounter due to their local and non-local interactions with the rest of the dislocation density and other barriers as they move across slip planes. The evolution of this resistance is determined mainly by the generation and annihilation of dislocation density during plastic deformation. A few constitutive models use dislocation densities as internal state variables (Cuitiño and Ortiz, 1992, 1993). These models have successfully captured the orientation dependence of the stress/strain behavior in copper and $L1_2$ intermetallic single crystals; however, the evolution of the dislocation state variables again follows phenomenological constitutive laws similar to those developed for strength-based internal variable formulations. Furthermore, only one scalar density is quantified for each slip system, and geometric aspects of the dislocation density on that system are not captured.

There are many advantages in adopting an internal state variable formulation for continuum crystal plasticity based on dislocation density. Transmission electron microscopy allows for direct observation of dislocation lines and structures in thin foils, and newer techniques such as orientation imaging microscopy can probe geometric properties of dislocation densities and the resulting lattice curvature (Adams et al., 1993; Sun et al.,

2000). In contrast, direct observation of slip-system strength is not possible, so strength must be inferred from difficult latent hardening experiments.

Dislocation mechanics provides physical laws and conservation equations on which to base density evolution equations, directly. The strength of the state can be thought of as a projection of the dislocation (structural) state of the material in stress space. With sufficient information concerning details of such structure/strength projections, along with the underlying dislocation-mechanics-based models of structural evolution, the phenomenological hardening relationships most often used in continuum formulations can be supplanted. Furthermore, recent experiments have demonstrated that many aspects of the length-scale dependence of plastic behavior in crystalline materials (Fleck et al., 1994; Stölken and Evans, 1998; Nix and Gao, 1998) relate to geometrically necessary dislocations, polar dislocation densities needed to maintain lattice compatibility and impose lattice curvature (Ashby, 1970). Incorporation of geometrically necessary dislocation density into working plasticity models has been accomplished using hybrid strength-density models (Dai et al., 2000; Arsenlis and Parks, 2000) or phenomenological extensions of pre-existing strength-based models (Fleck et al., 1994; Shu and Fleck, 1999; Acharya and Beaudoin, 2000). Construction of a general [dipolar] dislocation-density-based state variable model for scale-independent (macroscopic) crystal plasticity, as proposed here, has the advantage of seamless generalization to encompass scale-dependent material behavior by accounting for the evolution of polar dislocation populations (Arsenlis and Parks, 1999).

A compelling argument for a continuum crystal plasticity formulation based on dislocation density internal variables is the potential to incorporate it within a multi-scale modeling framework. Recently, dislocation dynamics has emerged as an important tool in modeling the motion, evolution, and interaction of discrete dislocations (Kubin et al., 1992; Van der Giessen and Needleman, 1995; Kubin et al., 1998; Zbib et al., 1998; Schwarz, 1999; Shenoy et al., 2000; Groma and Bakó, 2000); however, to date dislocation dynamics has been limited to extremely small plastic strains, $\varepsilon \approx 10^{-3}$, and relatively small total densities, $\rho \approx 10^{14}$ m^{-2}. Yet virtually none of the progress in dislocation dynamics has translated into continuum crystal plasticity formulations. The statistical results available from many-body dislocation dynamics simulations have largely been under-exploited in terms of the evolution of the dislocation density, the mean mobility of the density, and the mean properties of the dislocation population over the history of deformation. While it is unclear how such information could be incorporated into strength-based constitutive models of continuum crystal plasticity, a dislocation density-based model has the potential to connect discrete dislocation simulations to continuum plasticity by capturing the evolution of the density and its mean properties.

Here we develop a continuum constitutive model based on internal variables characterizing crystallographic dislocation density. The dislocation densities evolve in accordance with simple laws in dislocation mechanics, such as the continuity of dislocation line and conservation of Burgers vector. With evolution laws for the structural state variables introduced, the slip-system deformation resistances are taken to be functions of the current dislocation state, obviating the need for phenomenological hardening equations. The model is applied to the orientation-dependent tensile behavior of single-crystal aluminum at room temperature.

2. Constitutive model

The dislocation density internal variable formulation may conceptually be separated into two parts: the kinematics and kinetics of crystallographic slip, resulting plastic deformation, and lattice reorientation; and the kinematics and kinetics associated with evolution of the dislocation density state in the crystal. The two parts are intimately related. The dislocation state affects the plastic response of the crystal, and the plastic response of the crystal drives the evolution of the dislocation state. In this section, basic relationships for crystallographic slip and dislocation density evolution, as well as links between them, are developed.

2.1. Single-crystal plasticity

The constitutive formulation of crystal plasticity described below is based on the developments of Asaro and Rice (1977). The deformation gradient, $\mathbf{F}$, mapping a reference configuration of the material to the deformed configuration, is multiplicatively decomposed into elastic ($\mathbf{F}^e$) and plastic ($\mathbf{F}^p$) factors, such that

$$\mathbf{F} = \mathbf{F}^e \mathbf{F}^p, \tag{1}$$

where $\mathbf{F}^p$, describing the effects of plastic deformation on an unrotated and undeformed crystal lattice, maps neighborhoods of the original configuration to an intermediate configuration, and $\mathbf{F}^e$ maps neighborhoods of the intermediate configuration to the deformed configuration. Typically, $\mathbf{F}^e$ involves small elastic stretches and arbitrary rigid-body rotations. With plastic deformation, $\mathbf{F}^p$ evolves according to the flow rule

$$\dot{\mathbf{F}}^p = \mathbf{L}^p \mathbf{F}^p, \tag{2}$$

where $\mathbf{L}^p$ is the plastic flow rate. In crystals, $\mathbf{L}^p$ is comprised of the superposition of the resolved crystallographic plastic shear rates, $\dot{\gamma}^\alpha$, such that

$$\mathbf{L}^p = \sum_\alpha \dot{\gamma}^\alpha \, \mathbf{m}_0^\alpha \otimes \mathbf{n}_0^\alpha, \tag{3}$$

where $\mathbf{m}_0^\alpha$ and $\mathbf{n}_0^\alpha$ are unit lattice vectors in the reference configuration corresponding to the slip direction and the slip plane normal direction, respectively, for a given slip system α.

An elastic strain measure, $\mathbf{E}^e$, corresponding to the Cauchy–Green strain with respect to the intermediate configuration, is defined as

$$\mathbf{E}^e \equiv \tfrac{1}{2}\{\mathbf{C}^e - \mathbf{I}_2\}, \tag{4}$$

where $\mathbf{C}^e = \mathbf{F}^{eT}\mathbf{F}^e$, and $\mathbf{I}_2$ is the second-order identity tensor. The stress measure $\bar{\mathbf{T}}$ is related to the Cauchy stress, $\mathbf{T}$, through the transformation $\bar{\mathbf{T}} = \det(\mathbf{F}^e)\mathbf{F}^{e-1}\mathbf{T}\mathbf{F}^{e-T}$. Stress is related to elastic strain by

$$\bar{\mathbf{T}} = \mathscr{L}[\mathbf{E}^e], \tag{5}$$

where $\mathscr{L}$ is the fourth-order tensor of crystallographic elastic moduli.

Connections between the single-crystal plasticity framework and dislocation-density state variables are made by (i) quantifying the effects of stress and density on the mobility of the densities, (ii) relating the conservative glide motion of the crystallographic densities to the shear rates in Eq. (3), and (iii) describing the evolution of dislocation density arising from the mobility of density.

2.2. Dislocation density mechanics

With the exception of Eq. (5), the relationships of the previous section were fundamentally based on the configurational geometry of a plastically deforming crystalline body. These considerations focused constitutive modeling to a simple linear relationship between stress and elastic strain measures. The remaining complexity lies in predicting the crystallographically resolved plastic strain rates, $\dot{\gamma}^\alpha$, for representative values of stress and material state, as well as defining the evolution of the state. The intrinsic geometry of dislocation density mechanics provides a framework for development of simple constitutive equations for density evolution and crystal plasticity.

The essential geometry of a dislocation line is its Burgers vector, $\mathbf{b}$, and unit tangent vector, $\mathbf{t}$. The Burgers vector gives the slip displacement in the lattice due to the line defect. Together, the two vectors give the polarity, right- or left-handed, of the dislocation line as well as its character (screw, edge, or mixed). The Burgers vector takes only discrete values related to the crystal lattice, whereas $\mathbf{t}$ may take any direction.

The arrangement of dislocation lines in a crystal is not arbitrary: conservation of Burgers vector and continuity of dislocation line must be maintained. Dislocation lines cannot terminate within an otherwise perfect crystal. Rather, they must end on a free surface, a grain boundary, another set of dislocations, or some other type of defect. If a dislocation ends on another set of dislocations at a node, the combined Burgers vector of the set, be it one line or many, must have the same Burgers vector as the first dislocation, thereby conserving the total Burgers vector.

A density of dislocation lines, defined as the total length of dislocation line (of specified Burgers and tangent vectors) within a unit volume, must follow the same physical laws governing individual lines. In representing a group of dislocation lines as a density, information about the spatial correlation of lines within the volume is lost. However, conservation of Burgers vector can be extended to a density of dislocations (Arsenlis and Parks, 1999), restricting the spatial correlation of dislocation densities. Within the current internal variable framework, this conservation principle forms a basis for the density evolution equations.

On a macroscopic scale, and at ambient temperatures, the evolution of dislocation density is controlled by two physical processes: the generation of new density, and the annihilation of existing density. Both processes rely on conservative motion of dislocations through the crystal. Generation of density can be considered in two parts: nucleation and growth. Nucleation of density is controlled by the presence of discrete sources such as the famous Frank–Read source, and other such configurations whereby planar dislocation loops are nucleated. Since dislocation density does not capture the spatial correlation of dislocation lines within a reference volume, it also does not correlate with the existence (or not!) of the various source configurations within the

volume. We assume that such sources do exist if non-zero dislocation density is found within the volume. Expansion of these (pre-)nucleated loops by dislocation glide will be primarily responsible for the increase of dislocation line length within the volume ("growth" of density) and for the corresponding crystallographic shear resulting from their collective motion. The annihilation of density will be primarily controlled by close encounters of dislocation line segments of the same character but opposite polarity. The line segments are eliminated, reducing the total density. This density recovery mechanism forms the basis for annihilation of density in the model.

2.2.1. Generation of dislocation density

During crystallographic slip, dislocations move across the slip planes to accomplish the plastic deformation, but in doing so, they must increase the total dislocation line length in order to maintain line continuity and conserve Burgers vector. The simplest illustration of these concepts is the expansion of a planar dislocation loop of area A_s, embedded within representative volume V. The plastic shearing rate $\dot{\gamma}$ due to expansion of the loop is

$$\dot{\gamma} = \frac{\dot{A}_s |\mathbf{b}|}{V}, \tag{6}$$

where $\dot{A}_s$ is the rate of change in the slipped area within the loop (Argon, 1996). Along with the increase in slipped area, the perimeter also increases, generating more dislocation density within the volume. Changes in dislocation line length cannot be expressed in terms of the change in the slipped area because different configurations of the boundary can contain equal areas (and therefore equal shears), but unequal perimeters (and therefore unequal dislocation densities). However, if the outward displacement of the dislocation line were known as a function of its Burgers vector and tangent, then not only would the change in the slipped area be known, but so would the increase of the dislocation length, as a function of Burgers vector and tangent.

The continuous space of dislocation tangents makes such a general description difficult. If the tangent space is restricted to a discrete set of values, the topology of dislocation loops within the crystal becomes fixed, and expressions for rates of increase of discrete dislocation density become tractable. Consider the idealized expanding dislocation loop in Fig. 1. This discretization of tangent space is by no means the only possible discretization of a planar loop, but it is the simplest discrete loop geometry able to motivate equations for dislocation generation. The loop is composed of positive and negative edge dislocation segments of equal length, and positive and negative screw dislocation segments, also of equal length, arranged to form a closed loop. This loop discretization has been previously described (Lardner, 1974); however, previously developed density evolution equations differ significantly from those presented here. From the simple schematic in Fig. 1, it is evident that outward motion of the screw dislocation segments increases the length of both edge dislocation segments, and outward motion of the edge dislocations increases the length of the both screw dislocation segments. For this simple case, the time rate of change of the dislocation line lengths,
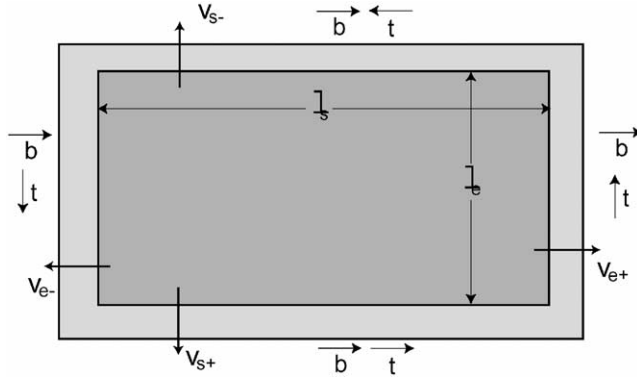
Fig. 1. Schematic of an expanding dislocation loop idealized as a composition of discrete edge and screw line segments forming a closed loop.

l, becomes

$$\dot{l}_{e+} = \dot{l}_{e-} = v_{s+} + v_{s-}, \tag{7}$$

$$\dot{l}_{s+} = \dot{l}_{s-} = v_{e+} + v_{e-}, \tag{8}$$

where v is the outward velocity of the dislocation loop relative to the lattice, the subscripts e and s denote dislocation character (edge, screw), and the "+" and "−" denote dislocation polarity, (right-, left-handed). Note that the generation of dislocation lines conserves Burgers vector because equal line lengths of positive and negative dislocations are created, and the rate of generation is independent of the length of the moving dislocation lines. The time rate of change of the slipped area A_s is

$$\dot{A}_s = l_{e+}v_{e+} + l_{e-}v_{e-} + l_{s+}v_{s+} + l_{s-}v_{s-} \tag{9}$$

and is related to the plastic shearing rate through Eq. (6).

   Results of this simple model may be generalized and applied to populations of discrete dislocation segments. If dislocation density ρ is defined as the dislocation line length per unit volume of the crystal, the kinematic evolution equations for the generation of dislocation density become

$$\dot{\rho}_{s+}^{\alpha} = \dot{\rho}_{s-}^{\alpha} = \frac{\rho_{e-}^{\alpha}\bar{v}_{e-}^{\alpha}}{\bar{l}_{e-}^{\alpha}} + \frac{\rho_{e+}^{\alpha}\bar{v}_{e+}^{\alpha}}{\bar{l}_{e+}^{\alpha}}, \tag{10}$$

$$\dot{\rho}_{e+}^{\alpha} = \dot{\rho}_{e-}^{\alpha} = \frac{\rho_{s-}^{\alpha}\bar{v}_{s-}^{\alpha}}{\bar{l}_{s-}^{\alpha}} + \frac{\rho_{s+}^{\alpha}\bar{v}_{s+}^{\alpha}}{\bar{l}_{s+}^{\alpha}}, \tag{11}$$

where $\bar{v}$ is the average velocity of the dislocation population, $\bar{l}$ is the average segment length of the dislocation density, and the superscript α denotes the crystal slip system. The sign convention implied in the equations requires that all densities, average

velocities, and average lengths be positive. The ratio $\rho/\bar{l}$ yields the number density of dislocation segments per unit volume, and, as in the simple example, the rate of generation of dislocation density is independent of the total dislocation length. Burgers vector is again conserved, with equal densities of positive and negative sign being created. The configuration used to introduce the dislocation generation equations was a planar loop, but the geometry need not be so simple. The essential assumption is that the mobile segments terminate within the crystal at dislocation nodes. Motion of the dislocation segment away from those nodes would again require the moving segment to leave a dislocation dipole trail extending to the nodes.

The current tangent discretization motivates the density generation equations presented here. A different discretization of the dislocation tangent space would lead to similar, although different, evolution equations. The main requirement in choosing an appropriate discretization is that closed planar loops can be described by the discrete space of tangents. Density generation equations for other tangent sets could again be motivated by expansion of a single loop.

2.2.2. Shearing and dislocation density flux

The dependence of plastic shear rate on the dislocation density flux can be easily found by combining Eqs. (9) and (6), providing

$$\dot{\gamma}^{\alpha} = (\rho_{e+}^{\alpha} \bar{v}_{e+}^{\alpha} + \rho_{e-}^{\alpha} \bar{v}_{e-}^{\alpha} + \rho_{s+}^{\alpha} \bar{v}_{s+}^{\alpha} + \rho_{s-}^{\alpha} \bar{v}_{s-}^{\alpha}) |\mathbf{b}| \operatorname{sign}(\tau^{\alpha}), \tag{12}$$

where τ^{α} is the resolved shear stress on slip system α. Eq. (12) generalizes the classical result obtained by Orowan (1940). Even in this simple case, it is impossible to determine the rates of dislocation generation from the plastic strain rate alone because the shearing rate does not contain enough information to determine uniquely the velocities of each of the participating densities. The sign of shearing, and of segment velocity, is chosen to match that of the resolved shear stress.

2.2.3. Annihilation of dislocation density

Along with the generation of new density in the crystal, the annihilation of dislocation density occurs simultaneously. At relatively low densities, the generation of density dominates dislocation density evolution, but as density increases, annihilation processes become more prevalent. Many dislocation reaction processes can reduce dislocation density. In modeling dislocation annihilation within the discrete dislocation density basis considered, annihilation of each discrete density must be considered.

The simplest annihilation reaction is the meeting of two equal-length dislocation segments having the same tangent direction and opposite Burgers vectors; their (vanishing) reaction product gives no resultant contribution to either of the respective densities. A more general annihilation reaction occurs when, for example, two dislocation segments with different Burgers vector and tangent line combine to form a third dislocation segment of lower total energy than that contained in the two initial segments. All such possible reactions could be considered, but just as in the evolution equations for density generation, Burgers vector must again be conserved at both the dislocation line

and density scales. This restriction is most generally enforced by using the dislocation tensor. The dislocation density tensor Λ may be defined in the lattice configuration as:

$$\Lambda \equiv \sum_{\xi} \mathbf{b}_0^{\xi} \otimes \int_l \mathbf{t}_0^{\xi} \, \mathrm{d}\rho^{\xi}, \tag{13}$$

where $\mathrm{d}\rho$ is a differential length per unit volume of a dislocation line with Burgers vector $\mathbf{b}_0$ and unit tangent $\mathbf{t}_0$, for all dislocation segments ξ in the volume. For a discrete tangent basis, the line integral becomes a simple summation of the form:

$$\Lambda = \sum_{\xi} \rho^{\xi} \mathbf{b}_0^{\xi} \otimes \mathbf{t}_0^{\xi}. \tag{14}$$

Any set of density generation and annihilation evolution equations is constrained to conserve Λ. The generation equations previously discussed satisfied this condition implicitly by creating dipole density that does not alter Λ. Self-annihilation likewise removes dipole segments, leaving Λ unchanged. All allowable annihilation reactions conserve the dislocation tensor and decrease the lattice defect energy. In the current formulation, we assume that self-annihilation is the dislocation reaction responsible for the majority of density reduction.

Consider a single negative dislocation moving with a velocity, v_{rel}, relative to a field of positive dislocations of density ρ_+. If the positive field is randomly distributed, then the negative dislocation passes within a certain distance, R, of a positive dislocation at a frequency f given by

$$f = \rho_+ R v_{\mathrm{rel}}. \tag{15}$$

If there are N_-/V negative dislocations per unit volume moving through the positive field, and an average segment length of $\bar{l}_-$ is eliminated every time one of the dislocations passes within the distance above, then the rate of annihilation of the negative density becomes

$$\dot{\rho}_- = -\frac{N_- \bar{l}_-}{V} \rho_+ R v_{\mathrm{rel}}. \tag{16}$$

In Eq. (16), $N_- \bar{l}_-/V$ is equivalent to the density of negative dislocations, ρ_-. Also, the annihilation rate of the negative density equals the corresponding positive annihilation rate. The annihilation rates must be applied to all of the dislocation indices introduced in the generation evolution equations. For the pure edge and pure screw dislocation density discretization considered, the annihilation rates become

$$\dot{\rho}_{e+}^{\alpha} = \dot{\rho}_{e-}^{\alpha} = -\rho_{e+}^{\alpha} \rho_{e-}^{\alpha} R_e (\bar{v}_{e+}^{\alpha} + \bar{v}_{e-}^{\alpha}), \tag{17}$$

$$\dot{\rho}_{s+}^{\alpha} = \dot{\rho}_{s-}^{\alpha} = -\rho_{s+}^{\alpha} \rho_{s-}^{\alpha} R_s (\bar{v}_{s+}^{\alpha} + \bar{v}_{s-}^{\alpha}). \tag{18}$$

Without screw cross-slip or edge climb, the annihilating dislocations would have to lie in the same slip plane. Although cross-slip and climb are not addressed explicitly within the present model, the relative magnitudes of the capture radii, R_s and R_e, account for both processes implicitly. From Eqs. (10), (11), (17), and (18), generation

depends linearly on the density, while annihilation depends quadratically on the density. Furthermore, if there is no net polarity of the dislocation density in the initial state, polar densities of the same character will be equal for all time as determined through the generation and annihilation processes; the internal variable space may then be reduced by defining

$$\rho_{e}^{\alpha} = \rho_{e+}^{\alpha} + \rho_{e-}^{\alpha} = 2\rho_{e+}^{\alpha} = 2\rho_{e-}^{\alpha} \tag{19}$$

$$\rho_{s}^{\alpha} = \rho_{s+}^{\alpha} + \rho_{s-}^{\alpha} = 2\rho_{s+}^{\alpha} = 2\rho_{s-}^{\alpha} \tag{20}$$

and

$$\bar{l}_{e}^{\alpha} = \bar{l}_{e+}^{\alpha} = \bar{l}_{e-}^{\alpha}, \tag{21}$$

$$\bar{l}_{s}^{\alpha} = \bar{l}_{s+}^{\alpha} = \bar{l}_{s-}^{\alpha}. \tag{22}$$

2.2.4. Evolution of dislocation polarity

The generation and annihilation contributions to the density evolution equations alter neither the net polar dislocation density of any dislocation species, nor the resulting dislocation tensor. Additional density evolution equations that do modify polarity can be considered, based on (i) the divergence of dislocation density flux and (ii) plastic flow in the presence of non-vanishing net dislocation tensor (i.e., non-vanishing dislocation polarity).

At macroscopic length scales, the (non-polar) generation and annihilation equations dominate, and the polarity-changing contributions can be ignored. As the length-scale of observation (the representative material volume) becomes microscopic, of linear dimension a few microns or less, the accumulation/loss of polar density has been shown to be important in describing material behavior (Dai et al., 2000; Fleck et al., 1994; Stölken and Evans, 1998; Nix and Gao, 1998). In the current application of the model to the orientation-dependent behavior of single-crystal aluminum, the polarity of density is expected to be small compared to total density, and thus to have small effect on mechanical behavior; therefore, its contribution will be ignored. The inclusion of evolution equations that follow changing polarities of crystallographic density will be the focus of an upcoming study.

2.2.5. Summary of density evolution equations

The generation and annihilation evolution equations described are based mainly on density kinematics, and few constitutive assumptions have been introduced. The structure of the evolution equations introduced three internal modeling functions: the average dislocation velocity $\bar{v}^{\xi}$, the average dislocation length $\bar{l}^{\xi}$, and the capture radius R^{ξ}, for a dislocation density of index ξ. Material-specific behavior is introduced through specific functional forms for these three internal variables. In general, we assume that they depend on the dislocation density state, applied stress, crystal geometry, and absolute

temperature θ such that

$$\bar{v}^{\xi} = \hat{\bar{v}}^{\xi}(\rho^{\zeta}, \bar{\mathbf{T}}, \mathbf{b}_0^{\zeta}, \mathbf{t}_0^{\zeta}, \mathbf{n}_0^{\zeta}, \theta), \tag{23}$$

$$\bar{l}^{\xi} = \hat{\bar{l}}^{\xi}(\rho^{\zeta}, \bar{\mathbf{T}}, \mathbf{b}_0^{\zeta}, \mathbf{t}_0^{\zeta}, \mathbf{n}_0^{\zeta}, \theta), \tag{24}$$

$$R^{\xi} = \hat{R}^{\xi}(\rho^{\zeta}, \bar{\mathbf{T}}, \mathbf{b}_0^{\zeta}, \mathbf{t}_0^{\zeta}, \mathbf{n}_0^{\zeta}, \theta). \tag{25}$$

Along with the dislocation geometry contained in $\mathbf{b}_0^{\zeta}$ and $\mathbf{t}_0^{\zeta}$, another direction, $\mathbf{n}_0^{\zeta}$, which specifies the unit normal of the area swept by a moving dislocation, is included as part of the dislocation geometry.

Possible functional forms for the internal variables will be introduced in the next section as the model is applied to the orientation-dependent behavior of single-crystal aluminum in simple tension. The discrete dislocation density basis used to derive the evolution equations in this section will be used to capture the behavior of density in the crystal.

3. Application to single-crystal aluminum

Single-crystal aluminum was chosen as an application on which to test the density-based internal state variable model. Aluminum was chosen because its highly-symmetric crystal structure (FCC) leads to geometrically similar dislocation densities, and because aluminum and its alloys are widely used in engineering applications. Continuum simulations of FCC single crystals have dealt mainly with the plastic response of copper (Cuitiño and Ortiz, 1992; Bassani and Wu, 1991), and to our knowledge, there has been no successful continuum simulation of aluminum single-crystal plasticity. The mechanical behavior of single-crystal aluminum is quite different from that of copper. For reasons to be discussed in Section 4, mechanical behavior of single-crystal copper seems to be "easier" to simulate, but aluminum is much more difficult.

The first modeling step within the dislocation density framework is choosing a discretization of dislocation density. Since the model will be applied to single-crystal aluminum at room temperature, where aluminum cross-slips readily due to its high stacking fault energy, a total of 18 distinct dislocation (dipole) densities are used in the reduced basis. The Burgers vectors, as well as the tangent directions, are given in Table 1, relative to the cube directions. Of the 18 dislocations, 12 are pure edge, one for each $\langle 1\,1\,0 \rangle \{1\,1\,1\}$ slip system, and 6 are pure screw, one for each $\langle 1\,1\,0 \rangle$ Burgers vector. The screw densities are permitted to slip freely on both of the glide planes in which they reside. More generally, the total density may be considered composed of two populations of dislocations. The screw densities represent the fraction of the population that may cross-slip, while the edge densities represent the fraction of the population that cannot cross-slip.

3.1. Constitutive functions

Each crystallographically similar dislocation density has the same functional form and material constants for dislocation mobility, average length, and capture radius.

Table 1
Geometry of dislocation density discretization used to model aluminum single crystals.
($\hat{\mathbf{b}} \equiv \mathbf{b}/|\mathbf{b}|$)

ρ Index	$\hat{\mathbf{b}}$	$\mathbf{t}$	Slip system
1	$\frac{1}{\sqrt{2}}[1\,\bar{1}\,0]$	$\frac{1}{\sqrt{6}}[1\,1\,\bar{2}]$	B6
2	$\frac{1}{\sqrt{2}}[1\,0\,\bar{1}]$	$\frac{1}{\sqrt{6}}[1\,\bar{2}\,1]$	B4
3	$\frac{1}{\sqrt{2}}[0\,1\,\bar{1}]$	$\frac{1}{\sqrt{6}}[\bar{2}\,1\,1]$	B2
4	$\frac{1}{\sqrt{2}}[1\,1\,0]$	$\frac{1}{\sqrt{6}}[1\,\bar{1}\,2]$	A5
5	$\frac{1}{\sqrt{2}}[1\,0\,1]$	$\frac{1}{\sqrt{6}}[1\,2\,\bar{1}]$	A3
6	$\frac{1}{\sqrt{2}}[0\,1\,\bar{1}]$	$\frac{1}{\sqrt{6}}[2\,1\,1]$	A2
7	$\frac{1}{\sqrt{2}}[1\,1\,0]$	$\frac{1}{\sqrt{6}}[\bar{1}\,1\,2]$	D5
8	$\frac{1}{\sqrt{2}}[1\,0\,\bar{1}]$	$\frac{1}{\sqrt{6}}[1\,2\,1]$	D4
9	$\frac{1}{\sqrt{2}}[0\,1\,1]$	$\frac{1}{\sqrt{6}}[2\,1\,\bar{1}]$	D1
10	$\frac{1}{\sqrt{2}}[1\,\bar{1}\,0]$	$\frac{1}{\sqrt{6}}[1\,1\,2]$	C6
11	$\frac{1}{\sqrt{2}}[1\,0\,1]$	$\frac{1}{\sqrt{6}}[\bar{1}\,2\,1]$	C3
12	$\frac{1}{\sqrt{2}}[0\,1\,1]$	$\frac{1}{\sqrt{6}}[2\,\bar{1}\,1]$	C1
13	$\frac{1}{\sqrt{2}}[1\,\bar{1}\,0]$	$\frac{1}{\sqrt{2}}[1\,\bar{1}\,0]$	B6 & C6
14	$\frac{1}{\sqrt{2}}[1\,0\,\bar{1}]$	$\frac{1}{\sqrt{2}}[1\,0\,\bar{1}]$	B4 & D4
15	$\frac{1}{\sqrt{2}}[0\,1\,\bar{1}]$	$\frac{1}{\sqrt{2}}[0\,1\,\bar{1}]$	A2 & B2
16	$\frac{1}{\sqrt{2}}[1\,1\,0]$	$\frac{1}{\sqrt{2}}[1\,1\,0]$	A5 & D5
17	$\frac{1}{\sqrt{2}}[1\,0\,1]$	$\frac{1}{\sqrt{2}}[1\,0\,1]$	A3 & C3
18	$\frac{1}{\sqrt{2}}[0\,1\,1]$	$\frac{1}{\sqrt{2}}[0\,1\,1]$	C1 & D1

Here we elaborate the specific functional forms chosen for these functions in Eqs. (23)–(25).

3.1.1. Average mobility of density: Eq. (23)

The motion of individual dislocations during plastic deformation may be viewed as a percolation process in which dislocation segments follow a path of least resistance, subject to the local stresses applied to the line. For most of the time the segments are immobile, pinned by forest dislocations. With sufficient activation, such an obstacle can be overcome, thereby allowing the dislocation to move rapidly to the next set of obstacles. Assuming that the average dislocation velocity can be written for the density of line segments in an explicit form, the dislocation density mobility will be described by an activated glide model first proposed by Kocks et al. (1975). The average density mobility takes the following functional form:

$$\bar{v}_e^\alpha = v_{e0} \exp\left[-\frac{\Delta F_e}{k\theta}\left(1 - \left(\frac{|\tau^\alpha|}{s_{ep} + s_{ed}}\right)^{p_e}\right)^{q_e}\right], \tag{26}$$

$$\bar{v}_s^\alpha = v_{s0} \exp\left[-\frac{\Delta F_s}{k\theta}\left(1 - \left(\frac{|\tau^\alpha|}{s_{sp} + s_{sd}}\right)^{p_s}\right)^{q_s}\right], \tag{27}$$

where the subscripts e and s denote edge and screw, respectively. In Eqs. (26) and (27), v_0 is a reference velocity, ΔF is the activation energy required to overcome the obstacles to dislocation motion, k is Boltzmann's constant, τ is the resolved shear stress on the dislocation density glide plane, s_p is the intrinsic lattice resistance, s_d is the resistance due to interactions with forest dislocations, and the parameters p and q determine the influence of the applied stress on the activation energy. The resolved shear stress τ^α is a function of the applied stress and crystal geometry. For dislocation densities in slip-system α, and small elastic strains, the resolved shear stress is well-approximated by

$$\tau^\alpha \doteq (\bar{\mathbf{T}}) \cdot (\mathbf{m}_0^\alpha \otimes \mathbf{n}_0^\alpha), \tag{28}$$

accounting for elastic strain requires replacing $\bar{\mathbf{T}}$ with $\mathbf{C}^e \bar{\mathbf{T}}$ in Eq. (28) (Bronkhorst et al., 1992).

The dislocation resistance s_d is taken to be a function of the dislocation density state. Dislocation resistance is modeled as primarily due to forest dislocation density interactions; however, reactions between the glide dislocations and dislocations in parallel glide planes are taken into account. Although the latter dislocations do not pierce the glide plane, statistical densities of dislocations parallel to the glide planes increase the resistance to slip (Argon, 1969). The dislocation resistance takes the following functional form:

$$s_d^\xi = \mu |\mathbf{b}| \sqrt{\sum_\zeta G^{\xi\zeta} \rho^\zeta}, \tag{29}$$

where s_d^ξ is the resistance encountered by dislocation density of index ξ, μ is the shear modulus, and $G^{\xi\zeta}$ is a matrix detailing the strength of interactions between dislocations of index ξ and ζ. By considering the symmetry of the FCC crystal, and the types of junctions formed between different dislocations, $G^{\xi\zeta}$ can be filled with 6 independent coefficients, G_0–G_5 (Lomer, 1951; Kocks, 1959; Franciosi and Zaoui, 1982).

The first two coefficients, G_0 and G_1, account for in-plane interactions, and the other four coefficients, G_2–G_5, account for out-of-plane interactions. The G_0-coefficient describes the interaction between dislocations with the same Burgers vector and parallel slip planes (self-interaction); however, there is no resistance between edge and screw dislocations with the same Burgers vector on parallel slip planes. The G_1-coefficient describes the interaction between dislocations on parallel slip planes, but with different Burgers vectors. The other four interaction coefficients contain dislocation densities that pierce the planes of the gliding density.

Crystallographic dislocation densities have been defined as line length per unit volume, but an equivalent definition is the number density piercing a unit area whose normal parallels the dislocation tangent. The piercing density of dislocation density ρ^ζ with tangent line direction $\mathbf{t}_0^\zeta$ on a plane with unit normal $\mathbf{n}_0^\xi$ is $|\mathbf{n}_0^\xi \cdot \mathbf{t}_0^\zeta| \rho^\zeta$. The four coefficients describing interaction between the out-of-plane forest density and the glide dislocations must account for not only the strength of the interaction, but also the piercing density on the glide plane.

Table 2
Strength-interaction sub-matrix, $G^{\xi\zeta}$, for the edge dislocation interactions. The average segment length-interaction matrix, $H^{\xi\zeta}$ takes the same form, but with different values. The values used to model single-crystal aluminum are given below

$$[G^{\xi\zeta}]_{\substack{\xi=1,12 \\ \zeta=1,12}} = \begin{bmatrix} G_0 & G_1 & G_1 & G_4 & G_5 & G_3 & G_4 & G_3 & G_5 & G_2 & G_3 & G_3 \\ G_1 & G_0 & G_1 & G_5 & G_4 & G_3 & G_3 & G_2 & G_3 & G_3 & G_4 & G_5 \\ G_1 & G_1 & G_0 & G_3 & G_3 & G_2 & G_5 & G_3 & G_4 & G_3 & G_5 & G_4 \\ G_4 & G_5 & G_3 & G_0 & G_1 & G_1 & G_2 & G_3 & G_3 & G_4 & G_3 & G_5 \\ G_5 & G_4 & G_3 & G_1 & G_0 & G_1 & G_3 & G_4 & G_5 & G_3 & G_2 & G_3 \\ G_3 & G_3 & G_2 & G_1 & G_1 & G_0 & G_3 & G_5 & G_4 & G_5 & G_3 & G_4 \\ G_4 & G_3 & G_5 & G_2 & G_3 & G_3 & G_0 & G_1 & G_1 & G_4 & G_5 & G_3 \\ G_3 & G_2 & G_3 & G_3 & G_4 & G_5 & G_1 & G_0 & G_1 & G_5 & G_4 & G_3 \\ G_5 & G_3 & G_4 & G_3 & G_5 & G_4 & G_1 & G_1 & G_0 & G_3 & G_3 & G_2 \\ G_2 & G_3 & G_3 & G_4 & G_3 & G_5 & G_4 & G_5 & G_3 & G_0 & G_1 & G_1 \\ G_3 & G_4 & G_5 & G_3 & G_2 & G_3 & G_5 & G_4 & G_3 & G_1 & G_0 & G_1 \\ G_3 & G_5 & G_4 & G_5 & G_3 & G_4 & G_3 & G_3 & G_2 & G_1 & G_1 & G_0 \end{bmatrix}$$

Strength-interaction coefficients: $G_0 = 0.10$, $G_1 = 0.22$, $G_{i=2,5} = g_i|\mathbf{n}_0^\xi \cdot \mathbf{t}_0^\zeta|$,
where $g_2 = 0.30$, $g_3 = 0.38$, $g_4 = 0.16$, $g_5 = 0.45$.

Length-interaction coefficients: $H_0 = 0.00$, $H_1 = 0.00$, $H_{i=2,5} = h_i|\mathbf{n}_0^\xi \cdot \mathbf{t}_0^\zeta|$,
where $h_2 = 0.05$, $h_3 = 0.12$, $h_4 = 0.03$, $h_5 = 0.25$.

The interaction coefficient G_2 describes the interaction between dislocation densities with the same Burgers vector, but on a different slip plane (cross-slip interaction) given by $G_2 = g_2|\mathbf{n}_0^\xi \cdot \mathbf{t}_0^\zeta|$, where g_2 accounts for the strength of this interaction and $|\mathbf{n}_0^\xi \cdot \mathbf{t}_0^\zeta|$ accounts for the piercing density. Likewise, $G_3 = g_3|\mathbf{n}_0^\xi \cdot \mathbf{t}_0^\zeta|$ describes the interaction between dislocation densities resulting in a junction with a $\langle 1\,1\,0 \rangle$ Burgers vector in the slip planes of both of the dislocations involved (glissile junction). The remaining two coefficients represent dislocation interactions forming sessile junctions. The weaker of the two, the Hirth lock, is described by $G_4 = g_4|\mathbf{n}_0^\xi \cdot \mathbf{t}_0^\zeta|$, and the stronger of the two, the Lomer–Cottrell lock, is described by $G_5 = g_5|\mathbf{n}_0^\xi \cdot \mathbf{t}_0^\zeta|$. The six coefficients fill the strength interaction matrix according to the types of interactions anticipated between the gliding density and the forest density. Table 2 shows the arrangement of the six interaction coefficients in the strength sub-matrix for the edge dislocation interactions.

3.1.2. Capture radii: Eq. (25)

The dislocation capture radii R^ξ are simply chosen as two constant lengths, R_e and R_s; they describe the critical approach distance for annihilation between edge and screw dislocations, respectively. Two lengths are required because cross-slip of screw dislocations indicates that the screw density should have a larger capture radius than edge dislocations, which cannot cross-slip. The small edge capture radius is based on an assumed ability of edge dislocation segments on parallel planes to climb short distances toward one another.

3.1.3. Average segment length: Eq. (24)

Perhaps the average dislocation segment length is the most difficult constitutive function to understand and physically motivate. Considering again the "generation" evolution equations and their relationship with the plastic strain rate, the average dislocation segment length relates an increment of the plastic strain associated with a particular density species to an increment in density due to its glide motion. The functional form of the average segment length could in theory be directly determined by analyzing dislocation dynamics simulations from the viewpoint of this kinematic framework. The simulations conducted by Kubin and co-workers (Kubin et al., 1992, 1998) are probably the most applicable. In their simulations, the dislocation lines are discretized as a series of small edge and screw dislocation segments. Since the same discretization is used here, analysis of the dislocation evolution in their discrete simulations could lead to a functional form for the "average segment length". To our knowledge, dislocation dynamics researchers have not published such an analysis of dislocation evolution; therefore a simple functional form of the average segment length will be used.

The average dislocation segment length $\bar{l}^{\xi}$ is assumed to be solely a function of the dislocation density state. Dislocation segments may become trapped in sections of the crystal where the forest density is considerably greater than in the majority of the crystal. As the forest density increases, more sections of the dislocation loops may become trapped, and the average length of a dislocation segment decreases. Accordingly, the following functional form will be used to model $\bar{l}^{\xi}$:

$$\bar{l}^{\xi} = \left(\sum_{\zeta} H^{\xi\zeta} \rho^{\zeta} \right)^{-1/2}, \tag{30}$$

where $H^{\xi\zeta}$ is the average segment length interaction matrix. The $H^{\xi\zeta}$-matrix is assumed to be composed of six coefficients, H_0–H_5, that follow the same convention as those of the $G^{\xi\zeta}$-matrix, and are based on the type of interactions anticipated between the gliding dislocation and the forest density. Because the H_0 and H_1 coefficients detail interactions between dislocations in parallel planes, we set $H_0 = H_1 = 0$. The coefficients H_2–H_5 detail "segmenting" interactions with dislocations piercing the slip plane. These coefficients are determined by $H_{i=2,5} = h_i|\mathbf{n}_0^{\xi} \cdot \mathbf{t}_0^{\zeta}|$, where h_i quantifies the strength of segmentation interaction and $|\mathbf{n}_0^{\xi} \cdot \mathbf{t}_0^{\zeta}|$ quantifies the piercing dislocation density on the slip plane. Values of $H^{\xi\zeta}$ are, in principle, independent of the values in the strength interaction matrix, $G^{\xi\zeta}$, but the $H^{\xi\zeta}$-matrix takes the same form.

For concise reference, the complete set of equations used is summarized in the appendix.

3.2. Selection of material constants

The parameter space of the constitutive functions is large, and is able to provide a rich description of material behavior.

Most of the material constants may occupy only a limited range of values. Kocks et al. (1975) suggest that the activation energy ΔF should lie in the range $0.05 \leqslant$

Table 3
Material parameters used for single-crystal aluminum simulations

Elastic moduli	$C_{11} = 108$ GPa
	$C_{12} = 61.3$ GPa
	$C_{44} = 28.5$ GPa
	$\mu = 25.0$ GPa
Dislocation mobility	$v_{e0} = v_{s0} = 1$ m/s
	$\Delta F_e = \Delta F_s = 3.0 \times 10^{-19}$ J/atom
	$s_{ep} = s_{sp} = 2$ MPa
	$p_e = p_s = 1.1$
	$q_e = q_s = 0.141$
Capture radii	$R_e = 18.6$ nm
	$R_s = 93.0$ nm
Burgers vector	$|\mathbf{b}| = 2.863$ Å

$\Delta F/\mu b^3 \leqslant 2$. Likewise, the exponents p and q typically lie in the following ranges: $0 \leqslant p \leqslant 1$, and $1 \leqslant q \leqslant 2$.

The strength-interaction coefficients G_0–G_5 relate to forest interactions and the amount that a dislocation line bows before it can cut through an obstacle; therefore, G_0, G_1, and g_2–g_5 should all be less than unity. Furthermore, latent hardening experiments show that out-of-plane interactions should be stronger than the in-plane interactions, and a strength-interaction scale has been suggested by Franciosi and Zaoui (1982). The non-zero segment length interaction coefficients H_2–H_5 should also have a limited range of numerical values related to the strength-interaction coefficients. A general guideline is that $0 \leqslant H_i \leqslant G_i$ for all interactions. The values chosen for the strength-interaction coefficients and the average segment length coefficients are found in Table 2.

To further decrease the parameter space, edge and screw densities were given the same mobility. In the mobility functions, the values of the activation energy, ΔF, and the exponents controlling the stress dependence, p and q, were based on work by Balasubramanian and Anand (2000), in which values were determined from the temperature-dependence of the rate-dependent yield strength of polycrystalline aluminum. The remaining coefficients were determined by fitting the orientation-dependent stress/strain data of aluminum single crystals at room temperature, and by maintaining dislocation densities of the same magnitude as observed in experiments. Table 3 contains the remaining values of all constants used to model aluminum crystals.

3.3. Implementation and simulation details

The constitutive model for single-crystal aluminum described above was implemented into the commercially available FEM package ABAQUS/Standard as a user-defined material (Hibbitt et al., 1998), and was used with first-order brick (C3D8) elements to simulate the orientation dependence of the stress/strain behavior of aluminum single crystals subject to uniaxial tension at ambient temperature. The simulations were

Table 4
Euler angles used to simulate single crystals with $1°$ misorientation

Orientation	$\theta(°)$	$\phi(°)$	$\omega(°)$
$\langle 1\,1\,1 \rangle$	55.6430	135.5119	0.0000
$\langle 1\,0\,0 \rangle$	89.5774	90.9063	45.0000
$\langle 1\,1\,2 \rangle$	34.4494	−43.9860	90.0000
$\langle 1\,2\,3 \rangle$	36.6992	153.4349	180.0000

conducted with four different crystallographic orientations ($\langle 1\,1\,1 \rangle$, $\langle 1\,0\,0 \rangle$, $\langle 1\,1\,2 \rangle$, and $\langle 1\,2\,3 \rangle$) parallel to the tensile axis, and were compared to the experiments conducted by Kocks (1959) and Hosford et al. (1960). Both sets of experimenters documented slight misorientations (within two degrees) in the test crystals; therefore, slight initial misorientations were included in the simulations for those (nominal) orientations having more than one potentially active slip system. The crystals were misoriented by one degree so that one slip system had a higher initial Schmid factor than the others: Table 4 gives the Euler angles used in the simulations.

The specimen geometry used in the simulation had a square cross-section, similar to the low-aspect rectangular cross-sections of the experiments, and the ratio of the specimen length to width was 9. Boundary conditions simulated a finite crystal and corresponded to the loading descriptions of Kocks and Hosford et al. Lateral surfaces were traction-free, and end surfaces were required to remain perpendicular to the pulling direction and, on average, to remain aligned with the tensile axis.

The initial dislocation density was set to 4.16×10^{10} m^{-2} for each crystallographic edge dislocation density and to 8.33×10^{10} m^{-2} for each crystallographic screw dislocation density, such that the total initial density was $\rho_0 = 10^{12}$ m^{-2} ($\rho_0 b^2 = 8.2 \times 10^{-8}$). Isothermal simulations were conducted at room temperature (298 K) under a constant nominal tensile strain rate of 10^{-3} s^{-1}.

4. Simulation results and discussion

4.1. Summary of experimental observations

In three of the orientations considered, two or more slip systems are equally stressed if the crystal is perfectly aligned with the tensile axis. The $\langle 1\,1\,1 \rangle$ orientation has 6 equally favored slip systems, while $\langle 1\,0\,0 \rangle$ has 8 equally stressed systems. The $\langle 1\,1\,2 \rangle$ orientation has two highly stressed slip systems, and the $\langle 1\,2\,3 \rangle$ orientation has only one highly stressed slip system. The orientations of the specimens in the reported experiments deviated from the ideal orientation by no more than two degrees (Kocks, 1959; Hosford et al., 1960); however, with misalignment, the symmetry of the slip systems with the tensile axis was broken, leading to variations in the resolved stresses on the potentially active slip systems.

From X-ray and slip-trace analysis, as well as observations of the macroscopic deformation in the tensile specimens, even slight misorientation can have a pronounced effect
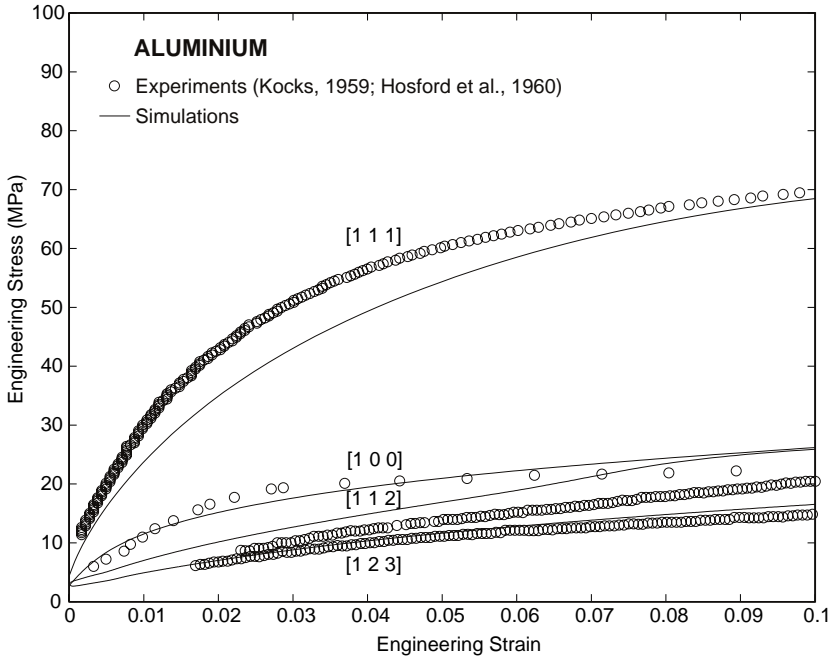
Fig. 2. Orientation-dependence of the stress/strain response of single-crystal aluminum observed during tensile experiments and calculated by finite element simulations.

on the deformation mode of the oriented crystals. The $\langle 1\,1\,1 \rangle$-oriented crystals deform "uniformly" by activating all six slip systems sufficiently to maintain the orientation of the $\langle 1\,1\,1 \rangle$ direction substantially parallel to the tensile axis. The $\langle 1\,0\,0 \rangle$ orientation follows a more complicated deformation path. Initially, all eight slip systems are active, but after a small amount of plastic strain ($\varepsilon \approx 0.01$), incremental cross-sectional deformation transitions from isotropic area reduction to a plane strain deformation in which the predominant crystallographic slip occurs on two pairs of cross-slip systems. The $\langle 1\,0\,0 \rangle$ direction remains aligned with the tensile axis during the deformation; however, during the plane strain deformation, there is significant asterism in the $\langle 1\,0\,0 \rangle$ pole that is not observed during the initial isotropic area reduction. The $\langle 1\,1\,2 \rangle$-oriented crystals deform plastically in a single-slip mode, with secondary slip on the other highly stressed slip system. The dislocations created during tensile deformation of $\langle 1\,1\,2 \rangle$-oriented crystals form Lomer–Cottrell locks, widely considered as the strongest dislocation junctions in FCC crystals. As a result, the $\langle 1\,1\,2 \rangle$-oriented crystals have the greatest plastic resistance among crystal orientations which primarily undergo single slip.

Tensile responses of the different crystallographic orientations of aluminum are effectively characterized by contrasting them with the corresponding behaviors of copper, the most widely tested and simulated FCC crystal. Fig. 2 depicts the tensile behavior of aluminum single crystals as determined by Kocks (1959) and Hosford et al. (1960), while Fig. 3 shows the tensile behavior of single-crystal copper
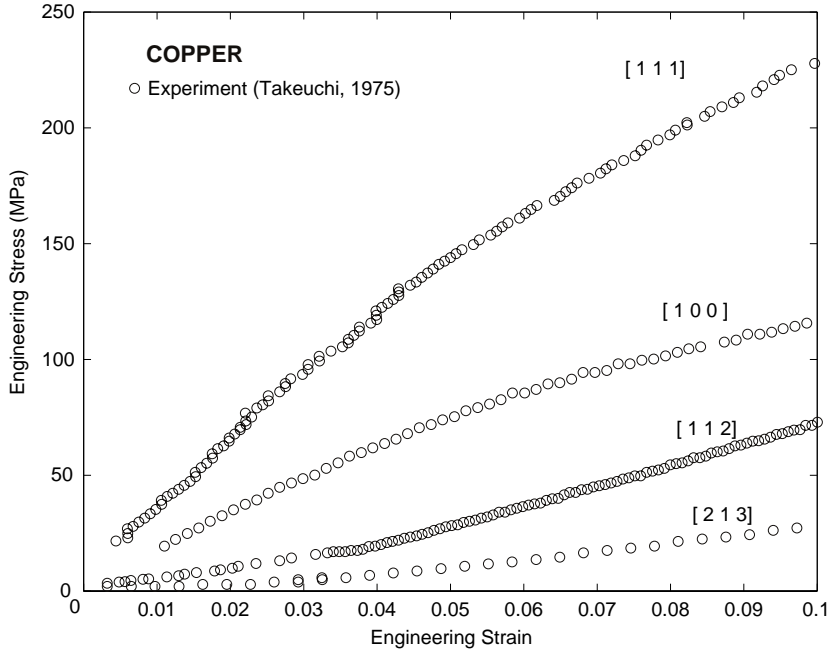
Fig. 3. Stress/strain response of copper single crystals during simple tension, for different orientations relative to the tensile axis.

specimens as determined by Takeuchi (1975). As in copper, the $\langle 1\,1\,1 \rangle$ orientation of aluminum has the highest initial hardening rate and reaches the highest stress levels. The curvature of the stress/strain curve in aluminum is much greater, and the saturation level of stress is reached at lower plastic strains. For small plastic strains, the $\langle 1\,0\,0 \rangle$ orientations of both aluminum and copper have high hardening rates. Copper crystals continue along that path, ultimately reaching stress levels roughly half of that reached in $\langle 1\,1\,1 \rangle$-oriented crystals. The $\langle 1\,0\,0 \rangle$-oriented aluminum behaves quite differently. As deformation transitions from isotropic area reduction to plane strain, the hardening rate drops dramatically, and the final stress levels reached are between one-fourth and one-third of those reached by the $\langle 1\,1\,1 \rangle$-oriented aluminum crystals. The tensile behavior of $\langle 1\,1\,2 \rangle$ and $\langle 1\,2\,3 \rangle$ orientations, both of which predominately deform by activating a single slip system, also differs qualitatively between copper and aluminum. Both of these orientations initially display Stage I hardening, with low hardening rates. Copper transitions to Stage II, with a high constant hardening rate, and then reaches Stage III hardening behavior, with falling hardening rates as the net rate of dislocation density accumulation begins to decrease. Aluminum transitions from Stage I directly to Stage III behavior at smaller strain levels than copper.

In the simulations conducted, the crystals were misoriented by 1° toward a single-slip orientation for the three multi-slip orientations, in an attempt to capture the initial conditions of the experiments. The stress/strain evolution in single crystals has been
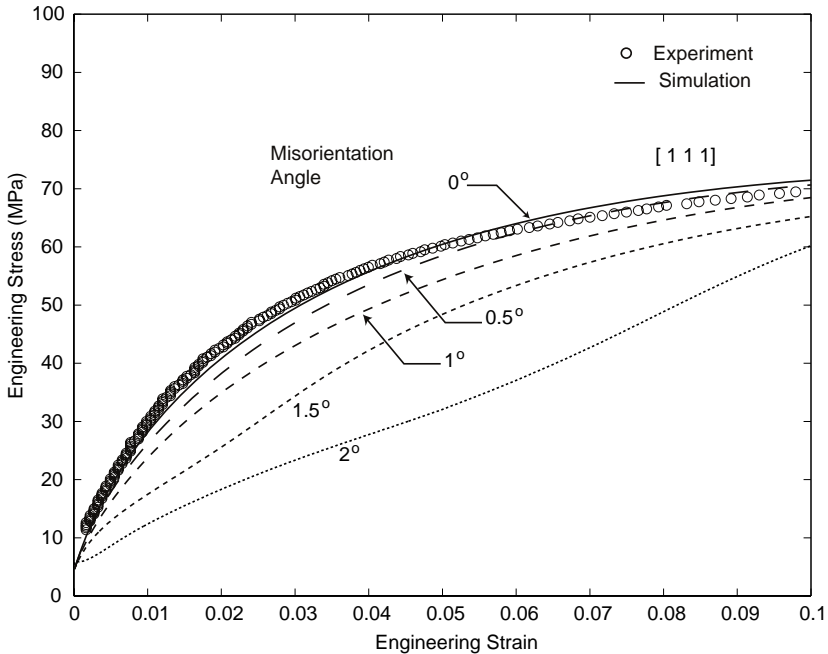
Fig. 4. Effect of initial misorientation on the stress/strain behavior of a nominally $\langle 1\,1\,1 \rangle$-oriented single crystal.

shown to be very sensitive to the accuracy of the initial orientation, especially for orientations in which two or more systems are (nominally) equally favored (Davis et al., 1957). The misorientations used in the simulations are unlikely to match those of the experiments, but we expect that our choices will permit us to obtain reasonable agreement with the experiments. The constants in the model were chosen to match the tensile deformation documented in the experiments, using 1° misorientations.

4.2. Comparison of simulations and experiments

Simulation results shown in Fig. 2 compare favorably with the experimentally determined stress/strain behavior for the different orientations. The sensitivity of the response to initial misorientation was investigated for the $\langle 1\,1\,1 \rangle$ and $\langle 1\,0\,0 \rangle$ multi-slip orientations. Results are shown in Figs. 4 and 5, respectively, for misorientations ranging from a perfectly oriented crystal to a maximum of 2°. The perfectly oriented $\langle 1\,1\,1 \rangle$ simulation traces the experimental data, and for misorientations of 1° or less, the agreement remains good. The perfectly oriented $\langle 1\,0\,0 \rangle$ simulation deviates from the experimental data of aluminum, and qualitatively resembles the behavior of single-crystal copper in the same orientation. The $\langle 1\,0\,0 \rangle$ simulation with 0.5° misorientation is close to that of the perfect orientation, but simulations for misorientations of 1° and 1.5° transition to lower hardening behavior after initially following the perfectly oriented simulation.
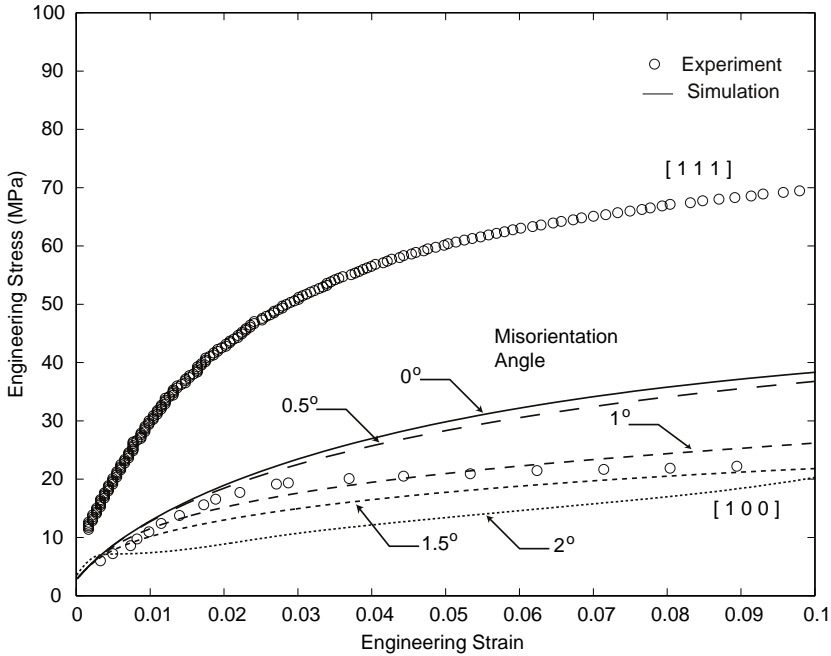
Fig. 5. Effect of initial misorientation on the stress/strain behavior of a nominally $\langle 1\,0\,0 \rangle$-oriented single crystal. Experimental data for $\langle 1\,1\,1 \rangle$ tension is shown for comparison only.

At 2° misorientation, both of these "multi-slip" orientations experience some degree of single slip.

The deformation modes in the $\langle 1\,1\,1 \rangle$- and $\langle 1\,0\,0 \rangle$-oriented crystals are interesting to compare and contrast because they have the most potentially active slip systems. The shearing rates on the active slip systems during the history of the deformation of the $\langle 1\,1\,1 \rangle$- and $\langle 1\,0\,0 \rangle$-oriented crystals are given in Figs. 6 and 7, respectively. In the figures, the Schmid and Boas notation is used for the 12 slip systems, where the letters A, B, C, and D denote the $(1\,\bar{1}\,\bar{1})$, $(1\,1\,1)$, $(\bar{1}\,\bar{1}\,1)$, and $(\bar{1}\,1\,\bar{1})$ slip planes, respectively; and the numbers 1, 2, 3, 4, 5, and 6 denote the Burgers vectors $[0\,1\,1]$, $[0\,\bar{1}\,1]$, $[1\,0\,1]$, $[1\,0\,\bar{1}]$, $[1\,1\,0]$, and $[\bar{1}\,1\,0]$, respectively.

The 1°-misoriented $\langle 1\,1\,1 \rangle$ crystal maintains slip activity on all six slip systems, and converges toward symmetric activation on all slip systems after initially diverging. Initially, all 8 potentially active systems contribute to plastic deformation in the 1°-misoriented $\langle 1\,0\,0 \rangle$ crystal, but the deformation mode quickly diverges to one in which 4 slip systems account for the majority of the plastic deformation. The four active systems comprise two pairs of slip-systems in which the screw dislocations may cross-slip. As a result, macroscopic incremental deformation appears isotropic in the early stages, and tends to plane strain after a small amount of tensile elongation.

The evolution of crystallographic dislocation density mirrors the shearing-rate histories of the crystals. Consider Figs. 8 and 9, which show the accumulation of nor-
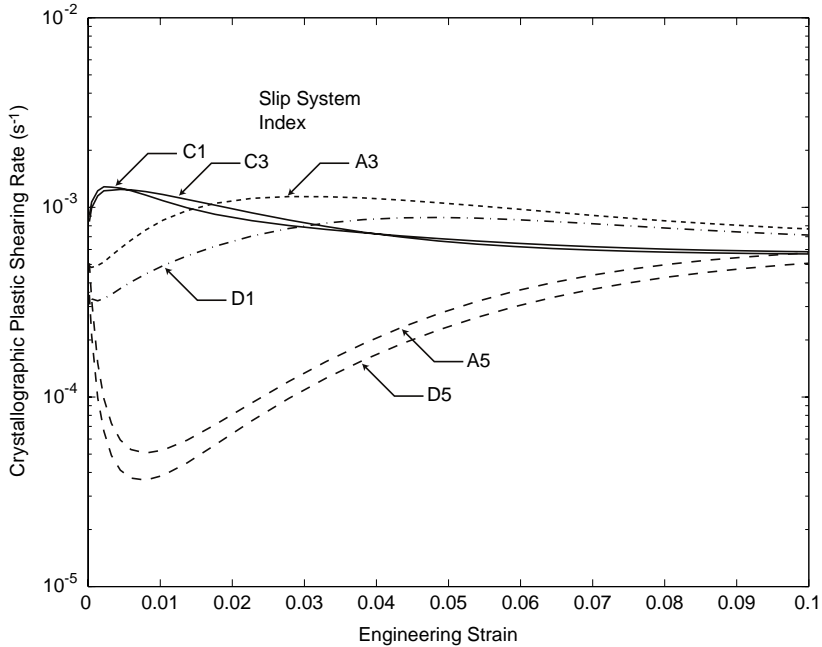
Fig. 6. History of crystallographic plastic shearing rates of the six potentially active slip systems of a ⟨1 1 1⟩-oriented single crystal. Initial misorientation is 1°.

malized crystallographic dislocation density during deformation of the ⟨1 1 1⟩- and ⟨1 0 0⟩-oriented crystals, respectively. In the ⟨1 1 1⟩-oriented crystal, the dislocation densities, which initially diverge due to the 1°-misorientation, converge at larger strains toward two values: one for the edge densities, and another for the screw densities. In Fig. 9, the evolution of dislocation density is plotted on a logarithmic scale for the 1°-misoriented ⟨1 0 0⟩ crystal. A rapid, near-homogeneous increase in dislocation density occurs in the first percent of strain; subsequently, the rate of increase in density drops dramatically. Over 10% tensile strain, dislocation density increases by roughly four orders of magnitude. Whereas in the ⟨1 1 1⟩ orientation the distribution of dislocation density was converging, the dislocation density in this orientation diverges. The most abundant crystallographic densities develop in the two pairs of slip systems accomplishing the plane strain deformation described above; the respective edge densities of these systems tend toward values somewhat greater than their screw densities.

Since both the edge and screw dislocation densities are calculated for each slip system, the general character of the dislocation density can be evaluated. Figs. 10 and 11 show the evolving character of the active dislocation densities during deformation of the ⟨1 1 1⟩- and ⟨1 0 0⟩-oriented crystals, respectively. The initial dislocation densities of each Burgers vector were split equally between edge and screw densities. As deformation progressed, the edge dislocation densities on active slip systems tend towards roughly 3.5 times the screw densities of the same Burgers vector. In the simulations,
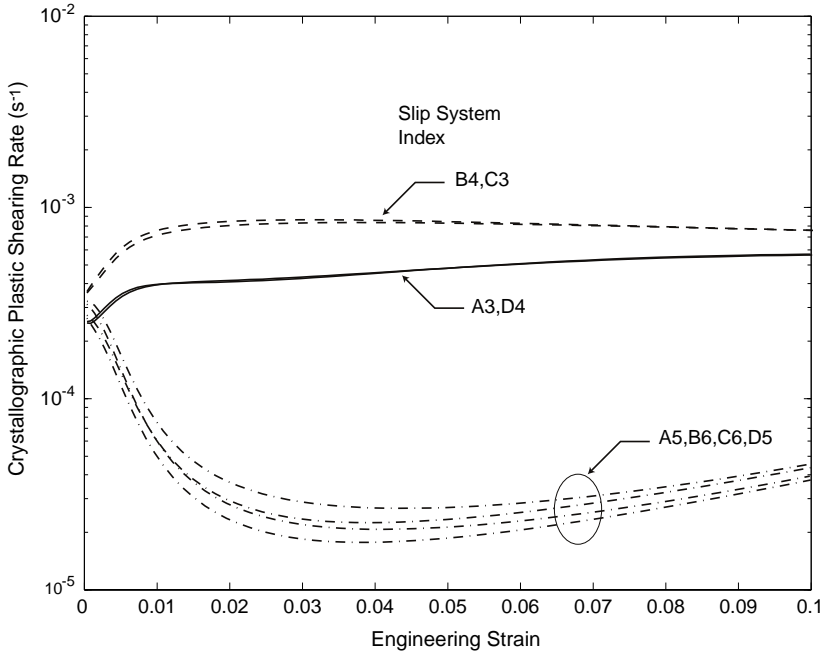
Fig. 7. History of crystallographic plastic shearing rates of the eight potentially active slip systems of a $\langle 1\,0\,0 \rangle$-oriented single crystal. Initial misorientation is 1°.

this asymptotic ratio depends mainly on R_e/R_s, the ratio of the edge and screw capture radii; however, other features within the model framework affect the character of the evolving density. For example, the ratio between the reference velocities, $\bar{v}_0$, in the edge and screw mobility equations, can alter the asymptotic character of the dislocation density. From the dislocation evolution Eqs. (10), (11), (17), and (18), it is evident that as the mobility ratio changes, the relative density of the "slower" species will increase, and as the ratio between the capture radii changes, the species with the larger capture radius will decrease. These results are robust and independent of the dislocation density profile set as the initial conditions of the simulation.

The magnitude of the dislocation density, along with its character, translates into the crystallographic strength of the crystal. Fig. 12 shows the evolution of resistance to dislocation motion on the potentially active slip systems for the $\langle 1\,1\,1 \rangle$- and $\langle 1\,0\,0 \rangle$-oriented crystals. Resistances in the $\langle 1\,1\,1 \rangle$ orientation increase smoothly, just as do the dislocation densities. Initially, the tensile stress and the crystallographic resistances are close in magnitude, while at 10% elongation, the crystallographic resistances are roughly 4.5 times the tensile stress. At 10% strain, the crystallographic strengths of the crystal are still increasing, even though the stress appears to be saturating. This separation occurs because as the dislocation density increases, the same plastic strain rate can be attained with lower average velocities, enabling the ratio of the applied stress to the crystallographic strength to decrease with increasing density. The history of the
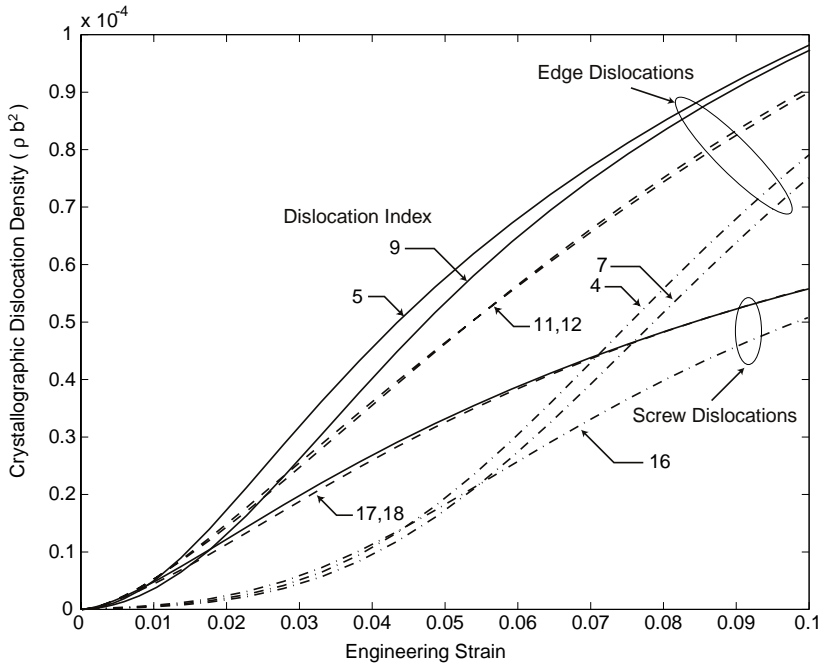
Fig. 8. History of crystallographic dislocation density generated during tensile elongation of a $\langle 1\,1\,1 \rangle$-oriented single crystal. Initial misorientation is 1°. Refer to Table 1 for the crystallographic details of each density index.

crystallographic strengths in the $\langle 1\,0\,0 \rangle$ orientation again reflects the bifurcation (rapid evolution of a symmetry-breaking initial imperfection) discussed earlier. The weakest systems are those with the most in-plane density, and the systems with the highest strengths, which become inactive, have the lowest in-plane (but highest piercing) densities. The spread in the strengths also demonstrates the strong off-diagonal dominance of the strength-interaction matrix associated with forest interactions.

The orientation-dependent behavior of single-crystal aluminum is quite different from the behavior observed in copper, as discussed earlier. The dislocation density model yields some insight into underlying reasons for the differing behaviors. The ability of screw dislocations in aluminum to cross-slip readily, in contrast to the inability of those in copper to do so, is one major factor in the difference. In the model, cross-slipping screw density motivated a large capture radius for screw dislocation annihilation. The large capture radius in turn led to a high curvature in the $\langle 1\,1\,1 \rangle$ stress/strain curve, and to the disappearance of Stage II hardening in the $\langle 1\,1\,2 \rangle$ and $\langle 1\,2\,3 \rangle$ orientations. Prominent dynamic recovery of dislocation density occurs at much lower density levels in aluminum than in copper.

The strongly different behavior of the $\langle 1\,0\,0 \rangle$-oriented aluminum crystal (as compared to copper) is a much more complicated story. As misorientation is applied to a nominally $\langle 1\,0\,0 \rangle$-oriented crystal, the transition from the activation of eight slip sys-
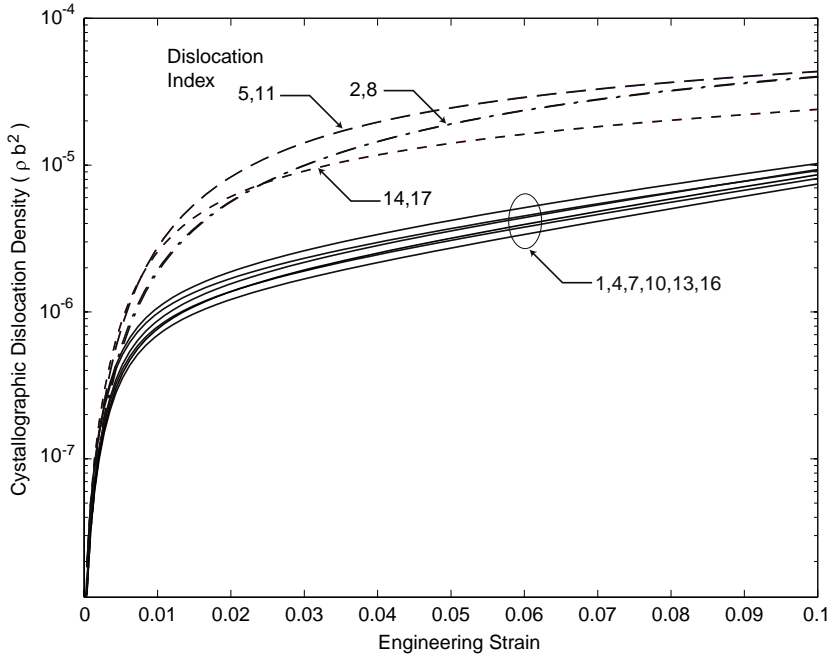
Fig. 9. History of crystallographic dislocation density generated during tensile elongation of a $\langle 1\,0\,0\rangle$-oriented single crystal. Initial misorientation is $1°$. Refer to Table 1 for the crystallographic details of each density index.

tems as found in copper, to the activation of four slip systems in aluminum, depends not only on the ability of screw dislocations to cross-slip, but also on the relative weakness of the Hirth lock as compared to the other out-of-plane dislocation interactions. The eight potentially active slip systems in the $\langle 1\,0\,0\rangle$ test comprise four pairs of cross-slip systems. With initial misorientation, one of the slip systems in each cross-slip pair has the higher Schmid factor, while the other of the pair has one of the lower Schmid factors of the eight active systems. The most active systems develop the largest dislocation densities. Cross-slip of the screw dislocations, however, increases mobile density on the cross-slip system pair member of lower Schmid factor, and promotes the increase of edge dislocation density on the latter cross-slip system. The evolution of dislocation density in Fig. 9 shows this mechanism. Considering the four terminally active systems, edge dislocation density on the two cross-slip systems of initially lower Schmid factor is lower than the corresponding screw dislocation density for strain less than $\sim 2.5\%$; but as the deformation proceeds, the edge density on these systems eventually exceeds their screw density, and ultimately it approaches the value of the edge density on the systems of higher initial Schmid factor. The transition from the activation of all eight slip systems to four slip systems would not be possible were it not for the relative weakness of the strength-interaction coefficient ($g_4 = 0.16$) associated with the Hirth lock, compared to the other out-of-plane strength interactions: ($g_2 = 0.30$,

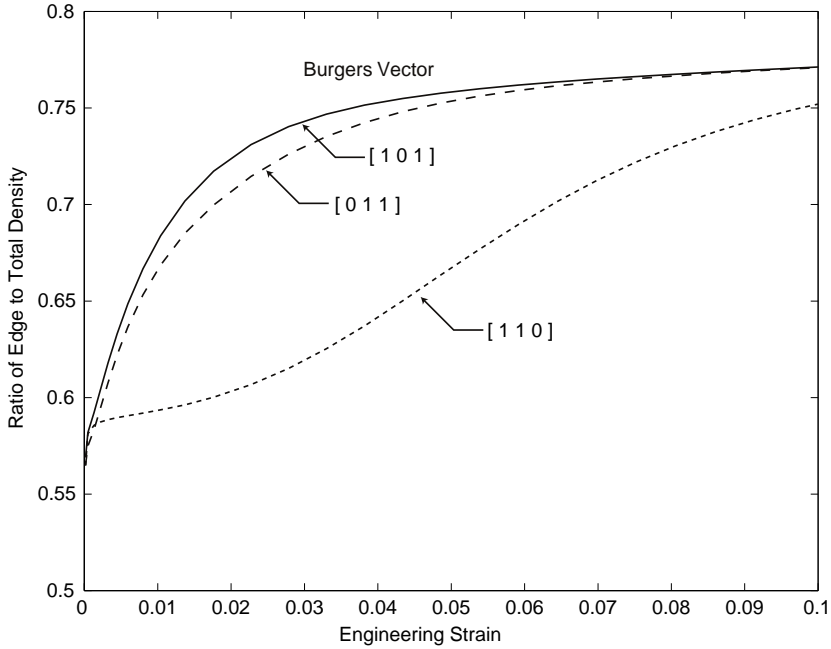Fig. 10. Ratio of edge dislocation density to the total density for each active Burgers vector during tensile elongation of a $\langle 1\,1\,1 \rangle$-oriented single crystal. Initial misorientation is 1°.

$g_3 = 0.38$, and $g_5 = 0.45$). The weak Hirth lock interaction coefficient provides plane strain deformation with a lower hardening rate than that of isotropic area reduction. Increasing the value of g_4 to 0.30, with all other parameters fixed, increases $\langle 1\,0\,0 \rangle$ strain hardening essentially to the perfectly oriented values shown in Fig. 5 and effectively suppresses the plane strain transition (Arsenlis, 2001). It is not clear how such physical understanding could be incorporated into a phenomenological hardening form in a strength-based internal variable model of crystal plasticity.

5. Conclusion

A dislocation-density-based internal state variable model for continuum crystal plasticity was presented. Based on core concepts in dislocation mechanics, such as the conservation of Burgers vector and the continuity of dislocation line, evolution equations for dislocation densities were constructed to account for bulk generation and annihilation processes. Mobility of dislocation density was connected to plastic straining through Orowan's relation, and to the evolution of dislocation density. The model required the infinite tangent space of dislocation lines to be discretized into a finite set. The density evolution equations introduced three classes of internal functions: namely, average dislocation mobility, average dislocation segment length, and capture radii for
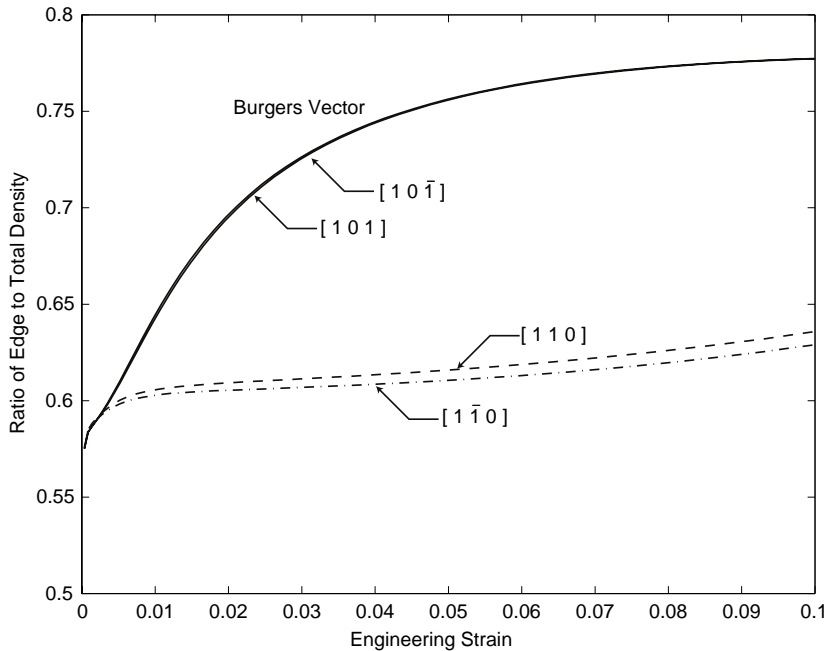
Fig. 11. Ratio of edge dislocation density to the total density for each active Burgers vector during tensile elongation of a $\langle 1\,0\,0 \rangle$-oriented single crystal. Initial misorientation is $1°$.

each dislocation density in the set. Through these three functions, the constitutive behavior of the crystalline material could be specified.

The orientation-dependence of single-crystal aluminum in tension illustrated features of the model. A discrete dislocation density set of 18 densities was used, comprising 12 pure edge dislocations and 6 pure screw dislocations. Forms for the three internal constitutive functions were suggested, yielding a set of material constants to be determined. Ideally, such constants could be determined from the results of dislocation density evolution emerging from detailed dislocation dynamics simulations, but such investigations have yet to be conducted. Constants in the example functional forms were determined from detailed comparisons of model behavior with the orientation-dependent tensile stress/strain data and deformation behavior of aluminum.

Linkage of the description and behavior of the microstructural state of a material to its plastic response is an important tool in quantitatively connecting underlying physics to both the mechanical behavior and the evolution of that microstructural state. The microstructural state, as captured by dislocation density distributions in crystalline materials, shows promise in facilitating such connections. Although dislocation microstructures have long been observed and known to be the root of the evolving mechanical properties in crystals, only recently have researchers been able to construct dislocation models to quantitatively connect microstructure to mechanical behavior. The dislocation-density-based model presented here retains and utilizes key microstruc-
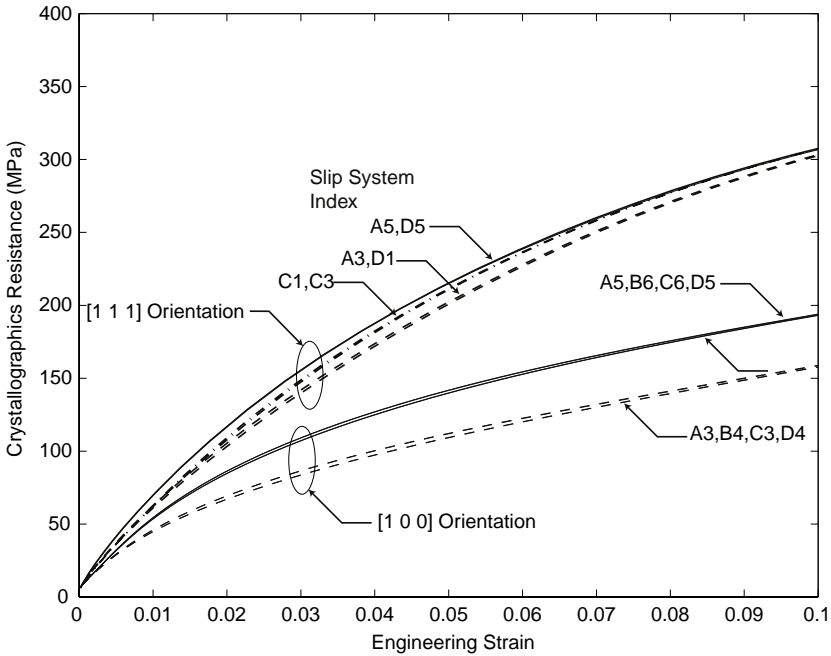
Fig. 12. History of the evolution of slip-system strengths in the potentially active systems during tensile elongation of $\langle 1\,1\,1 \rangle$- and $\langle 1\,0\,0 \rangle$-oriented single crystals.

tural information to model the mechanical behavior observed at macroscopic length scales.

Acknowledgements

Appendix A. Summary of constitutive equations

Elasto-plastic product decomposition of deformation:

$$\mathbf{F} = \mathbf{F}^{e}\mathbf{F}^{p}. \tag{A.1}$$

Flow rule:

$$\dot{\mathbf{F}}^{p} = \mathbf{L}^{p}\mathbf{F}^{p}, \tag{A.2}$$

$$\mathbf{L}^{\mathrm{p}} = \sum_{\alpha} \dot{\gamma}^{\alpha} \mathbf{m}_0^{\alpha} \otimes \mathbf{n}_0^{\alpha}. \tag{A.3}$$

Constitutive equation for Cauchy stress:

$$\bar{\mathbf{T}} = \frac{1}{2} \mathscr{L}[\mathbf{F}^{\mathrm{eT}} \mathbf{F}^{\mathrm{e}} - \mathbf{I}_2], \tag{A.4}$$

$$\mathbf{T} = \frac{1}{\det(\mathbf{F}^{\mathrm{e}})} \mathbf{F}^{\mathrm{e}} \bar{\mathbf{T}} \mathbf{F}^{\mathrm{eT}}. \tag{A.5}$$

Orowan's relation:

$$\dot{\gamma}^{\alpha} = (\rho_{\mathrm{e}}^{\alpha} \bar{v}_{\mathrm{e}}^{\alpha} + \rho_{\mathrm{s}}^{\alpha} \bar{v}_{\mathrm{s}}^{\alpha}) |\mathbf{b}_0^{\alpha}| \operatorname{sign}(\tau^{\alpha}). \tag{A.6}$$

Dislocation density evolution equations:

$$\dot{\rho}_{\mathrm{e}}^{\alpha} = \frac{2 \rho_{\mathrm{s}}^{\alpha} \bar{v}_{\mathrm{s}}^{\alpha}}{\bar{l}_{\mathrm{s}}^{\alpha}} - (\rho_{\mathrm{e}}^{\alpha})^2 R_{\mathrm{e}} \bar{v}_{\mathrm{e}}^{\alpha}, \tag{A.7}$$

$$\dot{\rho}_{\mathrm{s}}^{\alpha} = \frac{2 \rho_{\mathrm{e}}^{\alpha} \bar{v}_{\mathrm{e}}^{\alpha}}{\bar{l}_{\mathrm{e}}^{\alpha}} - (\rho_{\mathrm{s}}^{\alpha})^2 R_{\mathrm{s}} \bar{v}_{\mathrm{s}}^{\alpha}, \tag{A.8}$$

$$\bar{l}_{\mathrm{e}}^{\alpha} = \frac{1}{\sqrt{\sum_{\beta} (H_{\mathrm{ee}}^{\alpha\beta} \rho_{\mathrm{e}}^{\beta} + H_{\mathrm{es}}^{\alpha\beta} \rho_{\mathrm{s}}^{\beta})}}, \tag{A.9}$$

$$\bar{l}_{\mathrm{s}}^{\alpha} = \frac{1}{\sqrt{\sum_{\beta} (H_{\mathrm{se}}^{\alpha\beta} \rho_{\mathrm{e}}^{\beta} + H_{\mathrm{ss}}^{\alpha\beta} \rho_{\mathrm{s}}^{\beta})}}. \tag{A.10}$$

Constitutive equations for mobility of density:

$$\bar{v}_{\mathrm{e}}^{\alpha} = v_{\mathrm{o_e}} \exp\left[-\frac{\Delta F_{\mathrm{e}}}{k\theta} \left(1 - \left(\frac{|\tau^a|}{s_{\mathrm{p_e}} + s_{\mathrm{d_e}}} \right)^{p_{\mathrm{e}}} \right)^{q_{\mathrm{e}}} \right], \tag{A.11}$$

$$\bar{v}_{\mathrm{s}}^{\alpha} = v_{\mathrm{o_s}} \exp\left[-\frac{\Delta F_{\mathrm{s}}}{k\theta} \left(1 - \left(\frac{|\tau^a|}{s_{\mathrm{p_s}} + s_{\mathrm{d_s}}} \right)^{p_{\mathrm{s}}} \right)^{q_{\mathrm{s}}} \right], \tag{A.12}$$

$$s_{\mathrm{d_s}} = \mu |\mathbf{b}_0^{\alpha}| \sqrt{\sum_{\beta} (G_{\mathrm{ee}}^{\alpha\beta} \rho_{\mathrm{e}}^{\beta} + G_{\mathrm{es}}^{\alpha\beta} \rho_{\mathrm{s}}^{\beta})}, \tag{A.13}$$

$$s_{\mathrm{d_s}} = \mu |\mathbf{b}_0^{\alpha}| \sqrt{\sum_{\beta} (G_{\mathrm{se}}^{\alpha\beta} \rho_{\mathrm{e}}^{\beta} + G_{\mathrm{ss}}^{\alpha\beta} \rho_{\mathrm{s}}^{\beta})}, \tag{A.14}$$

$$\tau^{\alpha} \approx \mathbf{m}_0^{\alpha} \cdot \bar{\mathbf{T}} \mathbf{n}_0^{\alpha}. \tag{A.15}$$

References

Acharya, A., Beaudoin, A.J., 2000. Grain-size effect in fcc viscoplastic polycrystals at moderate strains. J. Mech. Phys. Solids 48, 2213–2230.

Adams, B.L., Wright, S.I., Kunze, K., 1993. Orientation imaging—the emergence of a new microscopy. Met. Trans. A 24, 819–831.

Argon, A.S., 1969. A statistical theory for easy glide II. In: Argon, A.S. (Ed.), Physics of Strength and Plasticity. MIT Press, Cambridge, MA, pp. 217–244.

Argon, A.S., 1996. Mechanical properties of single-phase crystalline media: deformation at low temperatures. In: Cahn, R.W., Haasen, P. (Eds.), Physical Metallurgy, 4th Edition. North-Holland, Amsterdam, pp. 1877–1955.

Arsenlis, A., 2001. Modeling dislocation density evolution in continuum crystal plasticity. PhD Thesis, MIT.

Arsenlis, A., Parks, D.M., 1999. Crystallographic aspects of geometrically-necessary and statistically stored dislocation density. Acta Mater. 47, 1597–1611.

Arsenlis, A., Parks, D.M., 2000. Three-dimensional modeling of the grain size dependent inelastic behavior of polycrystals. Int. J. Plast., in press.

Asaro, R.J., Rice, J.R., 1977. Strain localization in ductile single crystals. J. Mech. Phys. Solids 25, 309–338.

Ashby, M.F., 1970. The deformation of plastically non-homogeneous alloys. Philos. Mag. 21, 399–424.

Balasubramanian, S., Anand, L., 2000. Elasto-viscoplastic constitutive equations for polycrystalline fcc materials at low homologous temperatures, to be published.

Bassani, J.L., Wu, T.Y., 1991. Latent hardening in single crystals ii. Analytical characterization and predictions. Proc. Roy. Soc. London A 435, 21–41.

Beaudoin, A.J., Dawson, P.R., Mathur, K.K., Kocks, U.F., Korzekwa, D.A., 1994. Application of polycrystal plasticity to sheet forming. Comput. Methods Appl. Mech. Eng. 117, 49–70.

Becker, R., Panchanadeeswaran, S., 1995. Effects of grain interactions on deformation and local texture in polycrystals. Acta Metal. Mater. 43, 2107–2719.

Bronkhorst, C.A., Kalidindi, S.R., Anand, L., 1992. Polycrystalline plasticity and the evolution of crystallographic texture in FCC metals. Philos. Trans. Roy. Soc. London A 341, 443–477.

Cuitiño, A.M., Ortiz, M., 1992. Computational modelling of single crystals. Model. Sim. Mater. Sci. Eng. 1, 225–263.

Cuitiño, A.M., Ortiz, M., 1993. Constitutive modeling of $L1_2$ intermetallic crystals. Mater. Sci. Eng. A170, 111–123.

Dai, H., Parks, D.M., Nielson, G.N., 2000. Geometrically-necessary dislocation density in continuum crystal plasticity theory and FEM implementation, to be published.

Davis, R.S., Fleisher, R.L., Livingston, J.D., Chalmers, B., 1957. Effect of orientation on the plastic deformation of aluminum single crystals and bicrystals. Trans. AIME 209, 136–140.

Fleck, N.A., Muller, G.M., Ashby, M.F., Hutchinson, J.W., 1994. Strain gradient plasticity, theory and experiment. Acta Metal. Mater. 42, 475–487.

Follansbee, P.S., Kocks, U.F., 1988. A constitutive description of the deformation of copper based on the use of the mechanical threshold stress as an internal state variable. Acta Metal. Mater. 36, 81–93.

Franciosi, P., Zaoui, A., 1982. Multislip in FCC crystals, a theoretical approach compared with experimental data. Acta Metal. 30, 1627–1637.

Groma, I., Bakó, B., 2000. Dislocation patterning, from micro- to mesoscale description. Phys. Rev. Lett. 84, 1487–1490.

Hibbitt, Karlsson, Sorensen, 1998. ABAQUS Reference Manuals. Pawtucket, RI.

Hosford, W.F.J., Fleischer, R.L., Backofen, W.A., 1960. Tensile deformation of aluminum single crystals at low temperatures. Acta Metal. 8, 187–199.

Kocks, U.F., 1959. Polyslip in single crystals of face-centered cubic metals. PhD Thesis, Harvard University, Cambridge, MA.

Kocks, U.F., Brown, T.J., 1966. Latent hardening in aluminum. Acta Metal. 14, 87–98.

Kocks, U.F., Argon, A.S., Ashby, M.F., 1975. Thermodynamics and kinetics of slip. Progr. Mater. Sci. 19.

Kothari, M., Anand, L., 1998. Elasto-viscoplastic constitutive equations for polycrystalline metals, application to tantalum. J. Mech. Phys. Solids 46, 51–83.

Kubin, L.P., Canova, G., Condat, M., Devincre, B., Pontikis, V., Brechet, Y., 1992. Dislocation microstructures and plastic flow, a 3D simulation. Solid State Phenomena 23 & 24, 455–472.

Kubin, L.P., Devincre, B., Tang, M., 1998. Mesoscopic modeling and simulation of plasticity in fcc and bcc crystals, Dislocation intersections and mobility. J. Comput.-Aided Mater. Des. 5, 31–54.

Kumar, A., Dawson, P.R., 1998. Modeling crystallographic texture evolution with finite elements over neo-eulerian orientation spaces. Comput. Methods Appl. Mech. Eng. 153, 259–302.

Kumar, A.V., Yang, C., 1999. Study of work hardening models for single crystals using three dimensional finite element analysis. Int. J. Plast. 15, 737–754.

Lardner, R.W., 1974. Dislocation dynamics and the theory of the plasticity of single crystals. Z. Ang. Math. Phys. 20, 514–529.

Lomer, W.M., 1951. A dislocation reaction in the face-centered cubic lattice. Philos. Mag. 42, 1327–1331.

Marin, E.B., Dawson, P.R., 1998. On modelling the elasto-viscoplastic response of metals using polycrystal plasticity. Comput. Methods Appl. Mech. Eng. 165, 1–21.

Mathur, K.K., Dawson, P.R., 1989. On modeling the development of crystallographic texture in bulk forming processes. Int. J. Plast. 5, 67–94.

Nemat-Nasser, S., Ni, L.Q., Okinaka, T., 1998a. A constitutive model for fcc crystals with application to polycrystalline ofhc copper. Mech. Mater. 30, 325–341.

Nemat-Nasser, S., Okinaka, T., Ni, L.Q., 1998b. A physically-based constitutive model for bcc crystals with application to polycrystalline tantalum. J. Mech. Phys. Solids 46, 1009–1038.

Nix, W.D., Gao, H., 1998. Indentation size effects in crystalline materials, a law for strain gradient plasticity. J. Mech. Phys. Solids 46, 411–425.

Orowan, E., 1940. Problems in plastic gliding. Philos. Trans. Roy. Soc. London A 52, 8–22.

Qin, Q., Bassani, J.L., 1992. Non-associated plastic flow in single crystals. J. Mech. Phys. Solids 40, 813–833.

Schwarz, K.W., 1999. Simulation of dislocations on the mesoscopic scale, I. Methods and examples. J. Appl. Phys. 85, 108–119.

Shenoy, V.B., Kukta, R.V., Phillips, R., 2000. Mesoscopic analysis of structure and strength of dislocation junctions in fcc metals. Phys. Rev. Lett. 84, 1491–1494.

Shu, J.Y., Fleck, N., 1999. Strain gradient crystal plasticity, size-dependent deformation of bicrystals. J. Mech. Phys. Solids 47, 297–324.

Stölken, J.S., Evans, A.G., 1998. A microbend test for measuring the plasticity length scale. Acta Mater. 48, 5109–5115.

Sun, S., Adams, B.L., King, W.E., 2000. Observations of lattice curvature near the interface of a deformed aluminium bicrystal. Philos. Mag. A 80, 9–25.

Takeuchi, T., 1975. Work hardening of copper single crystals with multiple glide orientations. Trans. Jpn Inst. Metals 16, 629–640.

Van der Giessen, E., Needleman, A., 1995. Discrete dislocation plasticity—a simple planar model. Model. Sim. Mater. Sci. Eng. 3, 689–735.

Zbib, H.M., Rhee, M., Hirth, J.P., 1998. On plastic deformation and the dynamics of 3D dislocations. Int. J. Mech. Sci. 40, 113–127.